Title

Precipitation in High Purity Silicon Single Crystals

Authors

Nes, E
Washburn, J

Publication Date

1970-11-01

Submitted to Journal of
Applied Physics

UCRL-20354
Preprint

PRECIPITATION IN HIGH PURITY SILICON SINGLE CRYSTALS

E. Nes and J. Washburn

November 1970

AEC Contract No. W-7405-eng-48

LAWRENCE RADIATION LABORATORY
UNIVERSITY of CALIFORNIA BERKELEY

DISCLAIMER

UCRL-20354

PRECIPITATION IN HIGH PURITY SILICON SINGLE CRYSTALS

E. Nes and J. Washburn

Inorganic Materials Research Division, Lawrence Radiation Laboratory
Department of Materials Science and Engineering, College of Engineering
University of California, Berkeley

ABSTRACT

Precipitation in high purity, Lopex (low oxygen, dislocation free), silicon has been examined by x-ray diffraction topography and transmission electron microscopy. It has been found that the impurity concentration in the as-grown silicon crystals is sufficient to cause precipitation of a second phase if the specimens are annealed in the temperature range 700 to 1000°C, followed by a critical cooling rate. The precipitating phase has been tentatively identified as α-Fe_3Si.

The precipitates appear in colonies. Each colony has a three-dimensional star-like configuration, where the different arms are planar arrangements of precipitates enveloped by a dislocation loop. The precipitates have a volumetric shape and the dislocation loops are of interstitial edge type and both a/2 <110> and a <100> Burgers vectors are involved. The nucleation of colonies is heterogeneous and the presence of small silica particles as nucleation centers is suggested.

1. INTRODUCTION

This work was initiated by the discovery of a precipitation effect in undoped, low oxygen, dislocation free silicon samples, graded as of high purity. This precipitation effect exhibits striking similarities with that reported for copper in silicon.[1-6] It is well known that copper precipitates on dislocations during quenching of copper doped silicon crystals. This effect has been used as a dislocation decoration technique.[1] Transmission electron microscopy studies of foils made from silicon crystals saturated with copper at high temperatures, and subsequently quenched to room temperature, show that small spherical precipitates trail behind dislocation segments that have moved nonconservatively.[3] The most extensive work on copper precipitation has been carried out by Fiermans and Vennik.[4-6] These authors report that by quenching copper doped silicon crystals, star-like precipitates appear both on, and isolated from the grown in dislocations. A growth mechanism was proposed for the copper precipitates which is based on indentation at silica precipitates, followed by climb of dislocation loops. The climbing dislocations leave copper specks in their trail, thus forming precipitate colonies. The experimental techniques employed by Fiermans and Vennik were infrared microscopy,[4,5] x-ray diffraction topography[5] and electron microprobe analysis,[6] all techniques with very limited resolution. Thus, no observations related to dislocation structure and precipitate arrangements within the star branches were reported.

As the silicon crystals used throughout this work have a copper content too low to explain the present observations the formation of dendritic shaped precipitate colonies in the dislocation free silicon

single crystals must involve some other impurity. A mechanism similar to that for copper precipitation may apply also to other impurity atoms. No mechanism has been proposed for the growth kinetics of these colonies and on the nucleation of copper precipitate colonies the only suggestion has been that based on indentation of the silicon matrix by silica particles.[4,5] As no experimental evidence of silica precipitates in the as-grown material was presented by Fiermans and Vennik, this nucleation mechanism cannot be considered established.

The present investigation deals with the general morphology of the precipitate colonies as well as the nature of the precipitates. Further details concerning nucleation and growth of the precipitate colonies will be reported in a separate article. The experimental techniques used in this work have been conventional 100 kV and high voltage 650 kV electron microscopy and x-ray diffraction topography.

This precipitation effect occurs in as-grown materials intended for production of electronic components. However, it is beyond the scope of this work to determine or predict what influence this precipitation effect may have on the electronic properties.

2. EXPERIMENTAL

The silicon single crystals were obtained from Texas Instruments Company. The material was graded as Lopex (low oxygen, dislocation free silicon). The crystals were Czochralski grown in the form of cylindrical rods of 1 in. diam x 6 in, with [111] growth axis. The resistance of the crystals were 50 Ω-cm and the conductivity was n type.

Wafers with [111], [110] and [100] surface orientation were cut from the cylindrical rods. The specimens were annealed either in air, or in evacuated quartz capsules. The capsules had a diameter of approximately one inch, and the temperature close to the specimen was monitored during the heat treatment by a thermocouple sealed into the capsule. The annealing temperatures ranged from about 700°C up to about 1000°C. The annealing times varied from a few minutes up to 30 minutes. Specimens subjected to a wide range of cooling rates have been examined. For the encapsulated specimens different cooling rates were obtained by either having the capsules furnace cooled, air cooled outside the furnace or cooled by dropping the hot capsule into a liquid cooling agent. The cooling rates in these three cases were 0.3°C/sec, 6°C/sec and 12°C/sec respectively. Faster cooling was achieved for the specimens annealed in air. By air cooling of specimens wrapped in thin platinum foils, cooling rates of about 22°C/sec were obtained. The temperature was monitored by a thermocouple attached to the foil. Some specimens have been quenched into silicone oil. The exact cooling rate during quenching could not be measured directly, but theoretical estimates based on the heat conductivity and the geometrical shape of the specimens indicate that the cooling may have been as fast as 1000°C/sec or more.

The bulk distribution of precipitate colonies was studied by x-ray diffraction topography and by surface etching.[7] The x-ray diffraction technique of Lang[8] was applied. $Mo K\alpha_1$ radiation from a Hilger and Watts microfocus x-ray generator was used. The topographs were recorded on Ilford G5 nuclear emulsion plates with emulsion thickness 50μm.

The internal structure of individual colonies and the nature of the precipitates were studied by transmission electron microscopy. Both a Siemens Elmiscope electron microscope operating at 100 kV and a high voltage Hitachi electron microscope operating at 650 kV have been used. The micrographs presented in this paper will be marked (100 kV) or (650 kV) indicating micrographs taken at the standard or the high voltage microscope respectively.

3. EXPERIMENTAL RESULTS

No defects, precipitates or dislocations have been observed in the as-grown material, either by x-ray topography or by electron microscope observations. However, surface etching of as grown (111) wafers reveals a ring pattern as shown in Fig. 1a. The rings consist of a high density of triangular etch pits, Fig. 1b. By heating an as-grown specimen to a temperature in the range 700-1000°C for a few minutes, and then cooling at a moderately rapid rate, about 10°C/sec, a high density of precipitate colonies were introduced. Each colony appears as a small black dot on the x-ray topograph, Fig. 2a. As will be demonstrated in Section 3.2 each black dot in the x-ray topographs represents a colony of precipitates and dislocation tangels.

The precipitate colonies are formed during the cooling period. If the annealing temperature is above 700°C and the annealing time exceeds

a few minutes, then precipitation will occur if the cooling rate is at least 1°C/sec, but does not exceed several hundred degrees per second. Thus, the colony formation appears to be a critical cooling effect.

Precipitation has been observed in specimens cooled from temperatures as low as 723°C. For specimens cooled from temperatures below about 800°C the density of colonies is lower than in specimens cooled from higher temperatures. No systematic change in colony density, size and structure could be related to variation of the annealing temperature in the range 820°C up to 974°C. The general shape and the internal structure of the colonies were not influenced by varying the cooling rate from about 4°C/sec up to 22°C/sec, however, the colonies were somewhat bigger in specimens cooled at the 22°C/sec cooling rate.

3.1 Bulk Distribution of Precipitate Colonies

Figure 2a and b represent wafers cut normal and parallel to the [111] growth axis. The wafer cut normal to this axis, Fig. 2a, shows an even distribution of colonies, while the topograph from the wafer cut parallel to the growth axis, Fig. 2b, shows that the colonies are segregated into a stack of narrow planar areas, recorded as slightly curved lines on the photographic plate. The layers of high colony concentration are oriented normal to the growth axis, and the curvature of the layers is nearly symmetrical about the crystal ingot axis. The discs of high colony concentration had a thickness of about 100 μm and they were located a few 100 μm apart. The density of colonies within these areas was about 10^6-10^7 colonies/cm^3. A characteristic feature was the smaller colony sizes and eventually the colony free zone close to the cylindrical crystal surface, Fig. 2.

Long needle shaped precipitates have also been observed in some of the x-ray topographs, Fig. 3. The topograph in Fig. 3 shows two 1.2 mm long precipitates in the [011] direction, both extending from one surface to the other of the 1 mm thick wafer. Note the depleted zone surrounding these needle shaped precipitates.

Surface etching of a heat treated (111) wafer shows the same ring pattern as observed on the as-grown crystal surface (Fig. 1a). The defect colonies, however, give rise to etch tops or hillocks, rather than triangular etch pits, Fig. 1c. The layer distribution of colonies, as observed by x-ray diffraction topography, explains the characteristic etch pattern on the (111) crystal surfaces. The structure of some of the etch tops have been resolved as stars with branches in the <112> direction, Fig. 1d.

3.2 Geometrical Structure of the Precipitate Colonies

The transmission electron micrograph given in Fig. 4 shows a typical colony formation as found in a (111) foil. The colony shows a three dimensional star or dendritic shape, with each arm of the configuration consisting of a nearly planar arrangement of small precipitates. These precipitates appear as small black dots in the micrographs (Fig. 4). The geometry of the colonies is schematically outlined in the sketch in Fig. 5. Figure 5 illustrates a (111) foil with a colony in it. The electron microscope will record a projection of this colony. The transmission electron microscope requires thin foils. The actual thickness depends upon the beam voltage, being 1 μm at 100 kV and about 6 μm at 650 kV for silicon? As typical arm lengths for the configuration are up to 10 μm, only sections of a colony will appear

within the surfaces of a foil. Figure 5 shows that the different arms of a colony are on {110} or {100}type crystallographic planes. The {110} habit plane is verified by noting that these planes in a (111) foil either cut the surface in a <112> or a <110> direction. In a (111) foil a {100} plane also cuts the surfaces in a <110> direction. Therefore, to avoid any possibility of confusion the colonies would have to be examined in foils with another orientation. However, the width of the (100) section in a (111) micrograph will be about half that of (101) (provided both sections extend from surface to surface of the foil). The arm marked A in Fig. 4 is a {100} type, while all other arms in this micrograph are of the {110} type. The existence of {100} type arms is clearly demonstrated by the micrographs in Figs. 7 and 8, which show colonies in (110) foils. Figures 7 and 8 present colony arms either edge on, or inclined cutting the foil surface in the $[1\bar{1}0]$, or the $[00\bar{1}]$ direction respectively. Simple geometrical geometrical considerations show that this could only be a {100} arm.

It will be shown in Section 3.4 that the two different types of colony arms are also associated with dislocations of different Burgers vector. The dislocations involved in {110} and {100} type colony arms have $\frac{a}{2}$<110> and a <100> Burgers vectors respectively. As a colony arm is more generally described by its Burgers vector, rather than by the crystallographic plane of the configuration, the direction of the Burgers vector will be used to distinguish between the different types of arms. Thus, throughout the rest of this paper the colonies will be referred to

as <110> and <100> type arms.

Characteristic differences related to the dislocation structure, precipitate size and distribution are apparent between arms of the <110> and <100> type. In the <110> arms the precipitates appear to be nearly evenly distributed, and bounded by segments of a roughly circular dislocation loop. In the <100> type arms the enveloping dislocation forms long narrow branches in the orthogonal <110> directions, thus giving these arms a dendritic shape, (see the arm marked A in Fig. 4). The precipitates in <100> arms are much bigger in size, and a typical feature is that a precipitate is located at the tips of the dendrite branches.

3.3 The Precipitates

3.3.1 Identification

Selected area diffraction patterns from colonies in foils of (111) and (110) orientations have been examined. Only three different precipitate lattice reflections were detected, and the corresponding lattice spacings are listed in table I, column 4. These lattice spacings suggest the precipitating phase as cubic α-Fe_3Si The unit cube dimension in this iron silicide lattice is a = 5.655Å,[10] and the lattice spacings corresponding to different lattice reflections are given in table I, column 2. The fully ordered α-Fe_3Si unit cell has the face centered DO_3 structure,[10] the cell contains 16 atoms, 12 iron and 4 silicon atoms.

In order to interpret the electron diffraction experiments the structure factor for different α-Fe_3Si reflections have been calculated. The calculation is based upon the assumptions that the α-Fe_3Si phase

is fully ordered and of stoichiometric composition.[11,12] The DO_3 structure of α-Fe_3Si is face centered, thus the structure factor will be zero for planes of mixed indices. For the other cases the results are listed in table I column 3. As the diffracted intensities are proportional to the square of the structure factor this quantity is given in the table. Note that the [220], [400] and [422] iron silicide reflections have a substantially higher value for $|F_{hkl}|^2$ than any of the other reflections.

Although three reflections are too few for a complete structure analysis, it is interesting to note that the observed three reflections are the only ones with reasonably high structure factors, i.e. only the (220), (400), and (422) reflections, Table 3.1. A complete structure analysis would require a systematic examination of precipitates in a series of foil orientations. The present investigation includes only two orientations, i.e. (111) and (110). The (110) foils should be the most informative.

No other silicide or silicon compound, listed in the ASTM file, fits the observed d-values. Thus, the precipitating phase has been tentatively identified as α-Fe_3Si. According to the iron silicon phase-diagram the α-phase is stable only in the iron rich part of the diagram, and it follows that in this case the α-phase is in a metastable form.

3.3.2 Orientation Relationship

A dark field image and a selected area diffraction pattern from a <110> type colony arm in a (111) surface foil are shown in Fig. 6. Extra reflections corresponding to a precipitate lattice spacing of 2.00Å or 220 precipitate reflections are located close to and in the

directions of the $[02\bar{2}]$ and $[\bar{4}40]$ matrix reflections. Similar epitaxial orientation relationships between the precipitate and the matrix reflections have been observed also in other foil orientations. Thus, in the case of precipitates belonging to the <110> colony arms, the two cubic lattices involved, i.e. the DO_3 structure of the precipitates and the diamond structure of the matrix, both have the same orientation.

Precipitates belonging to the <100> type arms show a more complicated orientation relationship with the matrix. Figures 7 to 9 show <100> type arms in (110) and (111) foils. In each of these cases the orientation of the foil is such as to bring one reflecting plane in the precipitates into strong diffracting orientation. Figure 7 shows a [001] arm, edge on in a (110) foil. One strong precipitate reflection appears in the diffraction pattern (Fig. 7). This spot is located in a direction at an angle of 60° from the $[\bar{1}10]$ matrix direction. The extra spot corresponds to a precipitate lattice spacing of 2.00 $\pm$ 0.01Å, or a <220> precipitate reflection. Note how the precipitates light up in the dark field image of this reflection, Fig. 7b. Figure 8 gives a [010] arm in a (110) foil. One extra diffraction spot is located at an angle of 77° from the $[1\bar{1}\bar{1}]$ matrix direction. This spot also gives a 2.00 $\pm$ 0.01Å lattice spacing. Note that only the precipitates located on the branches in the $[10\bar{1}]$ direction light up in the precipitate reflection dark field image, Fig. 8b. A [001] colony arm in a (111) foil is presented in Fig. 9. A strong precipitate reflection appears in the $[22\bar{4}]$ matrix direction. This reflection corresponds to a precipitate lattice spacing of 1.41 $\pm$ 0.01Å, or a <400> precipitate

reflection. The three precipitate reflections in Figs. 7 to 9 define the complete orientation relationship between these precipitates and the matrix as follows:

$$(112)_p \;||\; (001)_m$$

$$[110]_p \;||\; [1\bar{1}0]_m \text{ or } [110]_m$$

where p and m indicate precipitate and matrix respectively. The $[1\bar{1}0]_p$ direction can be aligned with either of the two <110> directions in the (001) matrix plane. The direction selected will be given by the direction of the branch on which the precipitate is located. Thus, in a <100> type colony arm, precipitates on orthogonal <110> branches will have lattice orientations rotated 90° with respect to each other. This explains why only the $[10\bar{1}]$ precipitates contributed to the precipitate dark field contrast in Fig. 8.

This orientation relationship is illustrated in the stereographic projections in each of the Figs. 7 to 9. A <100> colony arm, seen edge on, in a (110) foil, will, according to the above orientation relationship, have the (111) precipitate planes parallel to the (110) matrix surface. This gives a $[20\bar{2}]$ precipitate reflection 60° from the $[\bar{2}20]$ matrix direction as observed in Fig. 7. For precipitates located on $[10\bar{1}]$ branches in a (110) foil, Fig. 8, the $[02\bar{2}]$ precipitate direction will appear in the (110) matrix plane 77° from the $[1\bar{1}\bar{1}]$ matrix reflection. This is in agreement with observations. Finally for the (001), $[\bar{1}10]$ precipitates in Fig. 9, the (110) precipitate planes will be parallel to the (111) foil surface so that $[00\bar{1}]_p \;||\; [11\bar{2}]_m$. This is also consistent with the diffraction spots that were observed.

3.3.3 Morphology

Figures 10a and b show details from <110> colony arms in (111) and (110) foils. In both micrographs the precipitate images have a distorted hexagonal form. In the (111) foil, Fig. 10a, the hexagonal sides are normal to <112> directions and in the (110) foil they are normal to <111> and <100> directions, Fig. 10b. The hexagonal forms in these two different projections suggest, together with the characteristic change in the orientation of the projected precipitate-matrix interfaces that the precipitates have a three-dimensional volumetric shape rather than being of a plate shape. These two projections suggest that the basic geometrical shape of the precipitates is a truncated cube with {100} and {111} faces as shown in Fig. 11. The [111] and [110] projections of this cube correspond to the precipitate images in the (111) and (110) foils respectively (Fig. 10a and b).

Figure 12a and b shows details from <100> colony arms in (110) foils. The precipitates in Fig. 12a are of the kind (001), $[1\bar{1}0]$, that is, precipitates on $[1\bar{1}0]$ dendrite branches belonging to a (001) colony arm seen edge on in a (110) foil. Figure 12b shows (010), $[10\bar{1}]$ precipitates. If the geometry of Fig. 11 is extended along one of the <110> axis, the resulting shape will describe these <100> type precipitates.

3.3.4 The Precipitate Strain Field

The precipitates belonging to <110> type arms usually exhibit strong strain contrast, Fig. 13. Close examination of the precipitate image in Fig. 13 shows a line of no contrast normal to the direction of the scattering vector (g-vector). Note how this line of no contrast rotates with the direction of g. This contrast effect

indicates that the precipitates are surrounded by a spherical stress field. This type of stress field is consistent with the cube-cube orientation relationship, Section 3.3.4, between the matrix and the precipitates. A strain field of spherical symmetry is expected.

The stress field surrounding the precipitates in the <001> arm in Fig. 14 gives rise to a nearly circular image when the g-vector is in the $(20\bar{2})$ or $(0\bar{2}2)$ direction. No strain contrast appears for the $(\bar{2}20)$ g-vector contained in the (001) plane. As will be discussed in detail in Section 3.4, this contrast variation is consistent with a stress field similar to that surrounding an edge dislocation loop. The contrast analysis given in Section 3.4 further shows that the precipitate stress field is compressive in nature. This stress field suggests a plate-shaped morphology of the precipitates. However, as demonstrated in the foregoing section, the precipitates have a more equiaxed shape. The strong 100 directional character of this strain field is probably caused by the special orientation relationship between the precipitates and the matrix, i.e. $(112)_p \,||\, (001)_m$.

3.4 Dislocation Structure

Figure 15a-c show three <220> two beam micrographs of a colony consisting of two <110> type arms in a (111) foil. The arms A-A and B-B are located on (110) and (011) planes respectively. Note that the dislocations are out of contrast in that arm which contains the g-vector. This contrast variation is consistent with the dislocations being in a pure edge orientation.

As demonstrated by the three <220> two beam reflections in Fig. 16a-c,

the dislocations within a <100> type colony arm are also of a pure edge character. The dislocation segments parallel to the g-vector are, as expected for a pure edge dislocation, out of contrast, while the segments normal to g have the characteristic double image.[14] This effect is even more pronounced in Fig. 14c.

No fringe contrast has been observed within the colony arms. This suggests that no stacking fault is involved. Therefore, the two different types of colony arms, i.e. <110> and <100> are probably associated with dislocations with a/2<110> and a<100> Burgers vectors respectively.

A very important result related to the nature of the dislocations is that the dislocation loops surrounding the precipitates are all of an interstitial character, i.e. each arm of a colony represents at least two extra planes of silicon atoms. Evidence for this can be obtained from Fig. 17 which shows a <100> arm. Changing the sign of s, where s is the deviation from the Bragg condition, in a two beam dark field case will cause the image of a dislocation to switch from one side to the other of the true position of the dislocation line,[15-18] By knowing the crystallographic plane of the colony arm this effect can be used to determine if the enveloping loop is of interstitial or vacancy type. The slope of the colony arm can also be determined by changing the sign of s, as $s > 0$, $s < 0$ bring the bottom and top of the foil into stronger contrast respectively.[19] Thus, the colony arm in Fig. 17 runs through the foil as indicated by the TOP and BOTTOM signs. By observing that the branches, marked A in Fig. 17 shrink from $s > 0$ to $s < 0$, it can be concluded that the enveloping dislocation loop is

of interstitial character.

In Section 3.3.4 above it was reported that the stress field surrounding precipitates belonging to <100> arms was of the same type as that of an interstitial dislocation loop. This is illustrated by the precipitate images, marked B in Fig. 17, which shrink when s is changed from $s > 0$ to $s < 0$.

4. DISCUSSION

The iron concentration in the silicon crystals used in the present investigation was less than 0.2 p.p.m.[20] This precipitation effect, however, can be explained in terms of iron precipitation even with an iron concentration as low as 0.02 p.p.m., which corresponds to the solute solubility in silicon at about 800°C.[21] Previous work on the solubility and diffusivity of iron in pure silicon is scarce.[22,23] The iron solubility in silicon as measured by Struthers[22] and Collins and Carlson[23] disagree by as much as two to three orders of magnitude for temperatures below 1200°C. However, as pointed out by Collins and Carlson who checked Struthers tracer experiments at 1200°C, the amount of iron used in the tracer experiments might have been insufficient to obtain the equilibrium solubility. Trumbore,[21] therefore, draws the solubility curve of iron in his review article on impurities in silicon arbitrarily to favor Collins' and Carlson's data.

Iron atoms diffuse in the silicon lattice with an activation energy of 0.86 eV,[22] and the diffusivity constant $D_0 = 6.20 \times 10^{-3}$ cm^2/sec. Collins and Carlson[23] indicate that two species of iron might be present; a fast and a slow diffusing. The fast and slow diffusing species are interpreted as iron atoms interstitially and substitutionally dissolved respectively.

4.1 General Model for the Growth Mechanism

As the lattice parameters and structure of a precipitating phase are generally different from that of the matrix, the growth of a precipitate usually causes a severe local strain. Exchange of point defects between the precipitate and the matrix can partially relieve the

mismatch. It has been pointed out[24-27] that when there are no dislocations, grain boundaries or other sources of vacancies the growth of a precipitate may cause the nucleation of a dislocation loop.

This theory will be applied to explain the formation of the present precipitate colonies. The proposed growth mechanism is schematically illustrated in Figs. 18a to d. The mismatch strain field is reduced by generation of vacancies at the particle matrix interface. This results in the nucleation of a small dislocation loop which grows out from the precipitate acting as a source of vacancies which move to the growing precipitate by pipe diffusion along the dislocation. As it climbs away from the initial precipitate the loop tends to act as a heterogeneous nucleation site for new precipitates,[28,29] Figs. 18c and d.

This simple model explains the following three fundamental characteristics of the colony branches.

(a) The nearly planar layers of precipitates that make up the colony arms.

(b) The presence of a surrounding dislocation loop.

(c) The interstitial edge character of the dislocation loop.

This model suggests that the number of atoms making up the extra layers of silicon in a colony corresponds to the number of vacancies absorbed by the growing precipitates. By observing the difference in the volume per silicon atom in the matrix and in the Fe_3Si, DO_3 structure, it follows that to account for the number of vacancies absorbed it is necessary to assume that the iron atoms are interstitially dissolved.

The growth model for the precipitates as presented above is too general to adequately explain all of the experimental observations.

To account for the development of the two types of colony arms, i.e., arms located on {110} and on {100} crystallographic planes, and to explain the characteristic differences in the geometrical shape of these arms, the nucleation and growth of the precipitate colonies are currently being studied in greater detail. Results will be reported in a separate paper.

4.2 The Nucleation Centers

The ring patterns on etched as grown crystal surfaces, Fig. 1a and b, suggest that very small precipitates or point defect clusters are present in the as grown state even though they have not been observed directly. As the bulk distribution of large precipitate colonies is identical to the distribution of these unidentified centers, this suggests that the nucleation of colonies is heterogeneous. In the following paragraphs the chemical nature of the nucleation centers will be discussed in some detail.

The periodic distribution of nucleation centers in slightly curved layers is interpreted as being a result of the growth process. The layers follow a growth ring pattern, with the curvature of the layers reflecting the instantaneous shape of the solid liquid interface. To retain this distribution during the slow cooling, which is used in production and through subsequent annealing treatments and to explain the formation of only very small defect clusters even after slow cooling, the diffusivity of the impurities involved must be very small. The diffusivity of iron atoms in silicon is relatively rapid, therefore, the possibility of having the iron atoms remain segregated into periodic layers can be disregarded. The long-needle-like precipitates, running from surface to surface of the 1 mm thick wafer, Fig. 3, show that

the precipitating iron atoms are evenly distributed, and independent of the distribution of nucleation centers.

Special attention will be focussed on the elements oxygen and carbon. The diffusion of these elements is very slow.[30-32] It is well established that both oxygen and carbon will be present in measurable quantities even in materials graded as of super purity.[6,33-35] Patel[33] has demonstrated that oxygen precipitation occurs during high temperature annealing (above 1000°C) of floating zone silicon crystals presumably "oxygen free." Fierman and Vennik[6] claim to have detected traces of carbon and oxygen at the centers of star-like copper precipitates formed during quenching of copper saturated low oxygen Lopex silicon. These observations demonstrate that even in the purest available silicon crystals, oxygen can be expected in concentrations exceeding 10^{17} atoms/cm^3.

Kaiser[36] reports that oxygen concentration in silicon crystals varies periodically in a band structure following the growth rings. By copper decoration of silicon crystals Dash[1] observed the same growth ring pattern. The zones were convex toward the melt and attributed to oxygen segregation. This growth ring structure is also consistent with the present observations. As no such distribution has been reported for carbon atoms in silicon, and as the formation of small silica (SiO_2) precipitates are observed[34] during high temperature annealing of silicon, it is believed that the nucleation centers for the iron precipitate colonies are small silica particles.

5. CONCLUSIONS

The experimental results and the subsequent discussion lead to the following conclusions.

1. The impurity concentration in as grown Lopex silicon crystals is sufficient to cause precipitation of a second phase if the specimens are annealed at temperatures above 700°C followed by a critical cooling rate.
2. The precipitating phase has been tentatively identified as α-Fe_3Si.
3. To account for the number of vacancies absorbed by the growing precipitates it is necessary to assume that the iron atoms are interstitially dissolved.
4. The precipitates appear in colonies. Each colony has a star or dendritic shape.
5. Each arm of a star represents a planar arrangement of precipitates, surrounded by an interstitial edge dislocation loop. Most colonies contain two different kinds of arms: associated with a <100> and a/2<110> dislocations respectively.
6. <110> type arms are nearly circular and lie on the {110} plane perpendicular to the Burgers vector of the dislocation. <100> arms are dendritic in shape with branches in <110> directions that lie in the plane perpendicular to the Burgers vector.
7. Orientation relationships:

   Precipitates belonging to <110> arms: A cube to cube symmetry. Cube axes parallel to those of the matrix. Precipitates belonging to <100> colony arms:

   $(112)_p \parallel (001)_m$

$[1\bar{1}0]_p \parallel [1\bar{1}0]_m$ or $[110]_m$

8. The colonies are distributed in a periodic array of layers which are normal to the growth axis. Colony density within the layers is $10^6 - 10^7$ cm^{-3}.

9. The precipitate colonies are nucleated heterogeneously. It is suggested that the nucleation centers are minute silica particles.

ACKNOWLEDGEMENTS

The authors are deeply grateful to Professor Gareth Thomas for many helpful comments. This work was done under the auspices of the Untied States Atomic Energy Commission through the Inorganic Materials Research Division of the Lawrence Radiation Laboratory.

Table I.

The lattice spacings for different crystallographic directions in the cubic α-Fe_3Si structure are given in column 2. The square of the structure factor is given in column 3, and the observed precipitate reflections are listed in the last column.

(hkℓ) Fe_3Si	$d_{hk\ell}$ [Å] Fe_3Si	$[F_{hk\ell}]^2$ [Å^2] Fe_3Si	Observed Precipitate reflections [A]
111	3.26	16	
200	2.83	15	
220	2.00	1840	2.00
311	1.71	13	
222	1.63	13	
400	1.41	920	1.41
422	1.16	560	1.16

REFERENCES

1. W. C. Dash, J. Appl. Phys. 30, 459 (1959); 31, 205 (1960).
2. G. H. Schwuttke, J. Electrochem. Soc. 108, 163 (1961).
3. H. Reiger, Phys. Stat. Sol. 7, 685 (1964).
4. L. Fiermans and J. Vennik, phys. stat. sol. 12, 277 (1965).
5. L. Fiermans and J. Vennik, phys. stat. sol. 21, 463 (1967).
6. L. Fiermans and J. Vennik, phys. stat. sol. 22, 463 (1967).
7. E. Sirtel and A. Adler, Z. für Metallk. 52, 529 (1961).
8. A. R. Lang, Acta Met. 5, 358 (1957); Acta Crystallogra. 12, 249 (1959).
9. G. Thomas, Phil. Mag. 17, 1097 (1968).
10. W. B. Pearson, Handbook of Lattice Spacings and Structures of Metals 2, (Pergamon Press, 1967).
11. M. C. M. Farquhar, H. Lipson and A. R. Weill, J. Iron Steel Inst. 152, 457 (1945).
12. F. Lihl and H. Ebel. Arch. Eisenhuttenw., 32, 489 (1961).
13. V. A. Phillips and J. D. Livingston, Phil. Mag. 7, 969 (1962).
14. P. B. Hirsch, A. Howie, R. B. Nicholson, D. W. Pashley and M. J. Whelan, Electron Microscopy of Thin Crystals (Butterworth, London 1965) p. 178.
15. P. B. Hirsch, A. Howie and M. J. Whelan, Phil. Trans. A 252, 499 (1960).
16. A. Howie and M. J. Whelan, Proc. Roy. Soc. A 262, 217 (1961).
17. M. F. Ashby and L. M. Brown, Phil. Mag. 8, 1083 (1963).
18. G. Thomas, Thin Films (American Society for Metals 1964) p. 227.
19. G. Thomas and W. L. Bell, phys. stat. sol. 12, 843 (1965).
20. Spark source mass spectrometry gave this result, analysis performed by Bell and Howell.

21. F. A. Trumbore, Bell Syst. Tech. J. 39, 205 (1960).

22. J. D. Struthers, J. Appl. Phys. 31, 2275 (1956).

23. C. B. Collins and R. O. Carlson, Phys. Rev. 108, 1409 (1957).

24. H. Brooks, Metal Interfaces (Cleveland: American Society of Metals 1952) p. 20.

25. R. G. Baker, D. G. Brandon and F. Nutting, Phil. Mag. 4, 1339 (1959).

26. J. W. Mitchell, J. Appl. Phys. 33, 406 (1962).

27. G. C. Weatherly, Phil. Mag. 17, 791 (1968).

28. J. W. Cahn, Acta Met. 5, 169 (1957).

29. R. B. Nicholson, Electron Microscopy and Strength of Crystals, G. Thomas and J. Washburn, editors, (Interscience, New York 1963) p. 861.

30. Corbett, McDonald and Watkins, J. Phys. Chem. Solids 25, 873 (1964).

31. R. C. Newmann and J. B. Willis, J. Phys. Chem. Solids 26, 375 (1965).

32. R. C. Newmann and J. Wakefield, J. Phys. Chem. Solids 19, 230 (1961).

33. J. R. Patel and B. W. Batterman, J. Appl. Phys. 34, 2716 (1963).

34. J. R. Patel, Disscussion, Faraday Soc. 38, 201 (1964).

35. W. Schenk, Solid State Electronics 8, 767 (1965).

36. W. Kaiser, Phys. Rev. 105, 1751 (1957).

FIGURE CAPTIONS

Fig. 1. Surfaces of etched (111) silicon wafers. (a and b) As grown material. (c and d) Heat treated specimens.

Fig. 2. X-ray diffraction topographs. (a) A (111) wafer (b) A (110) wafer cut parallel to the [111] growth axis.

Fig. 3. X-ray diffraction topograph of a (111) wafer showing needle-like precipitates in the [011] direction, $\vec{g} = \bar{2}20$.

Fig. 4. (100 kV) A colony in a (111) foil. The arm marked A is of <100> type, the other arms are of the <110> type.

Fig. 5. Sketch showing a colony in a (111) foil.

Fig. 6. (650 kV) (a) Dark field image of a <110> type colony arm in a (111) foil. (b) Selected area diffraction pattern showing extra precipitate reflections close to the $02\bar{2}$ and $\bar{4}40$ matrix reflections.

Fig. 7. (650 kV) A [001] colony arm seen edge on in a (110) foil. (a) Bright field image. (b) Dark field precipitate reflection image. The matrix and the precipitate orientations are given by the stereographic projections.

Fig. 8. (650 kV) A [010] colony arm in a (110) foil. (a) Bright field reflection (b) Dark field precipitate reflection image. The $02\bar{2}$ precipitate reflection can easily be seen in the diffraction pattern. The stereographic projections give the orientations of the matrix and the precipitate lattices.

Fig. 9. (650 kV) A [001] colony arm in a (111) foil. A strong $00\bar{4}$ precipitate reflection can be seen in the diffraction pattern. The orientation of the matrix and the precipitates is given by the stereographic projections.

Fig. 10. (650 kV) (a) Precipitates belonging to a $\langle 110 \rangle_\gamma$ type arm in a (111) foil. (b) Precipitates on a $\langle 110 \rangle_\gamma$ type arm in a (110) foil.

Fig. 11. The geometry of the <110> type precipitates.

Fig. 12. (650 kV) (a) Precipitates on a [001] type arm in a (110) foil. (b) Precipitates on a [010] type arm in a (110) foil.

Fig. 13. (100 kV) Two-beam bright field images of a <110> type arm in a (111) foil. Note how the line of no contrast in the precipitate image rotates with the $\vec{g}$-vector.

Fig. 14. (100 kV) Two-beam bright field micrographs of a [001] arm in a (111) foil. (a and b) The precipitates are surrounded by a nearly circular strain contrast image. (c) No precipitate strain contrast.

Fig. 15. (100 kV) Three two-beam bright field micrographs of two <110> type arms in a (111) foil. The A-A and B-B arms are located on (110) and (011) crystallographic planes respectively. The dislocations are out of contrast in the branch which contains the $\vec{g}$-vector.

Fig. 16. (100 kV) Two-beam bright field micrographs of a [001] type colony arm in a (111) foil. (a and b) Strong dislocation contrast. (c) The dislocation segments parallel to the $[1\bar{1}0]$ direction is out of contrast. Note the double image of the [110] segments.

Fig. 17. (100 kV) Two-beam dark field images of a [001] type arm in a (111) foil. (a) The configuration intersects the foil surfaces as indicated by the TOP and BOTTOM signs. Note how the branches marked A shrinks by changing from $s > 0$ to $s < 0$. The same

change in s brings the bottom and top of the foil into strong contrast respectively.

Fig. 18. Sketch showing the growth of a precipitate colony.

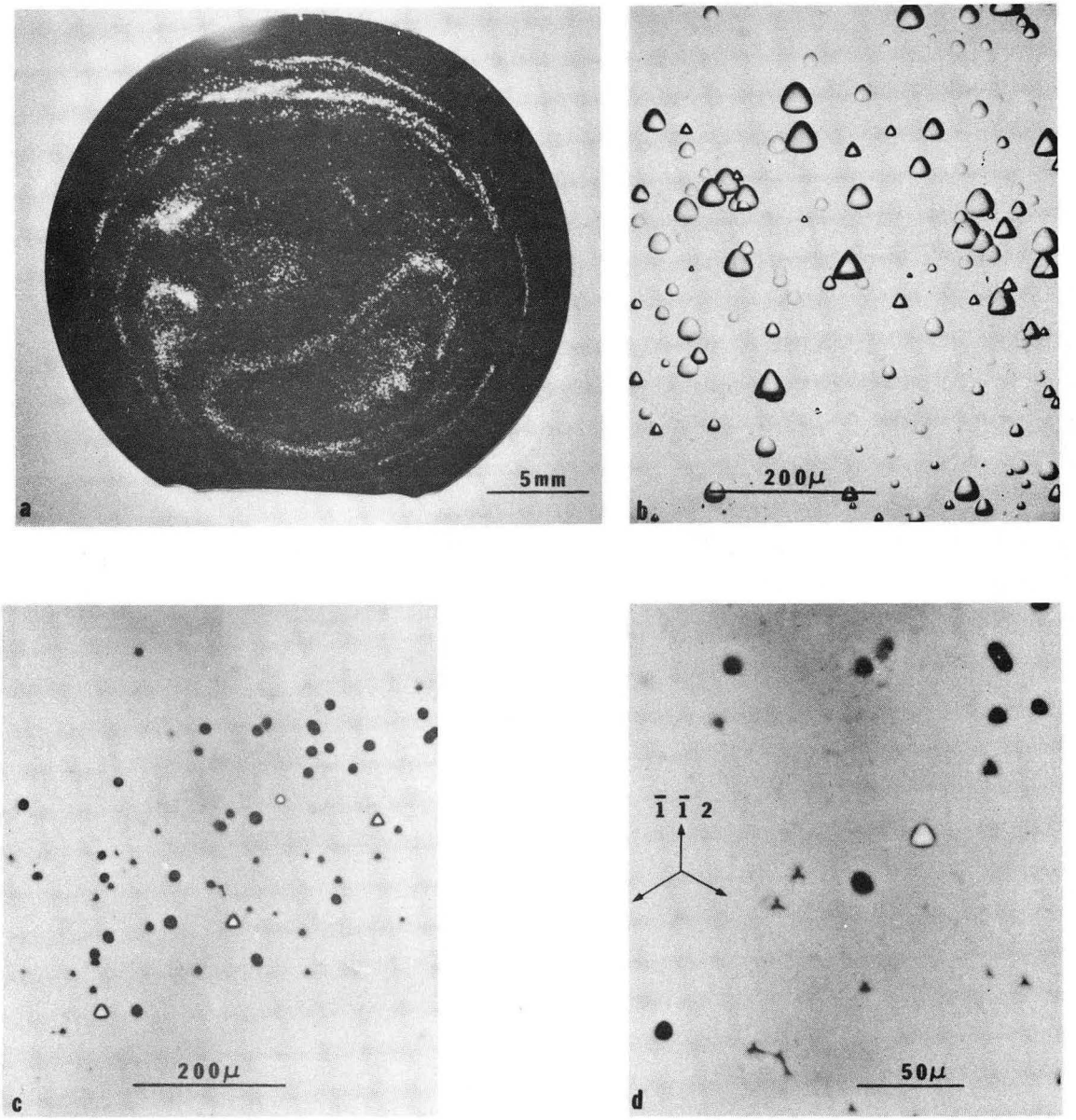

XBB 707-3130

Fig. 1

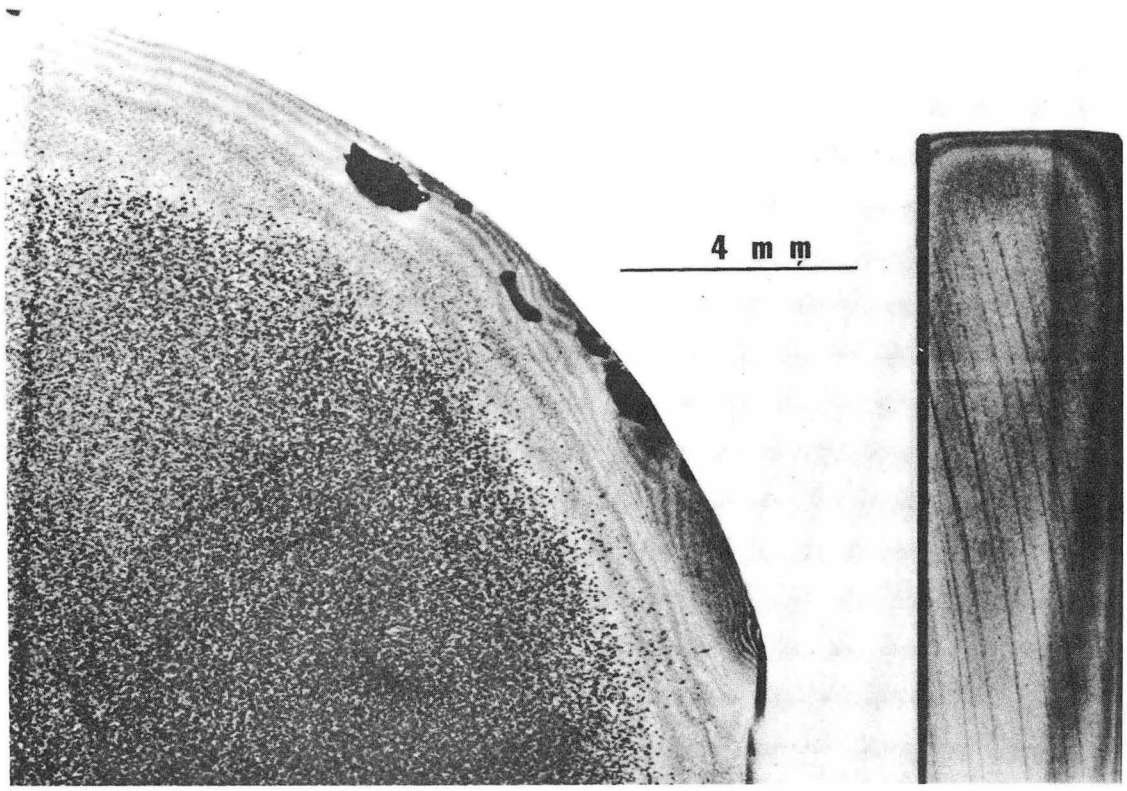

XBB 7010-4445

Fig. 2

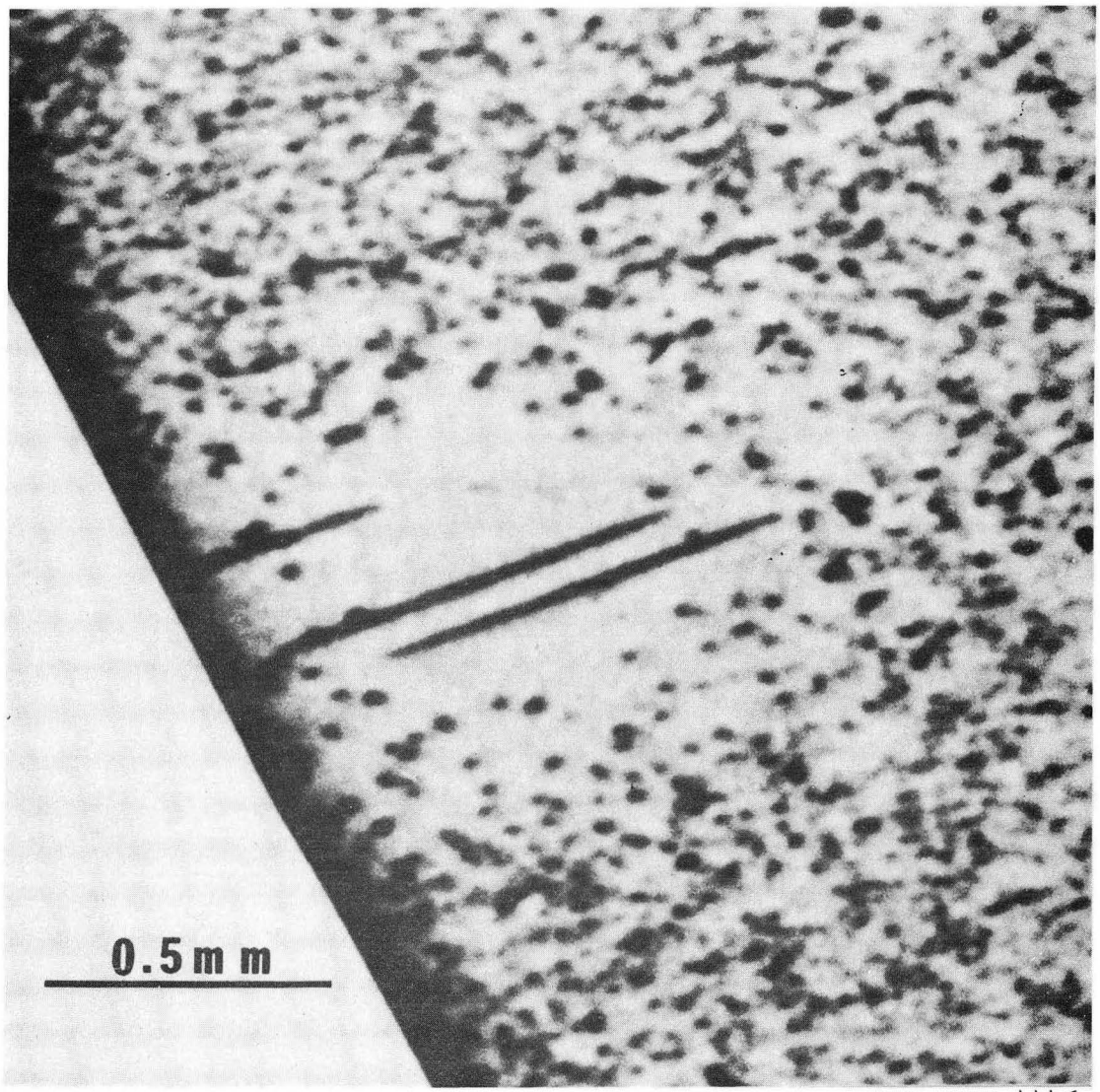

XBB 7010-4446

Fig. 3

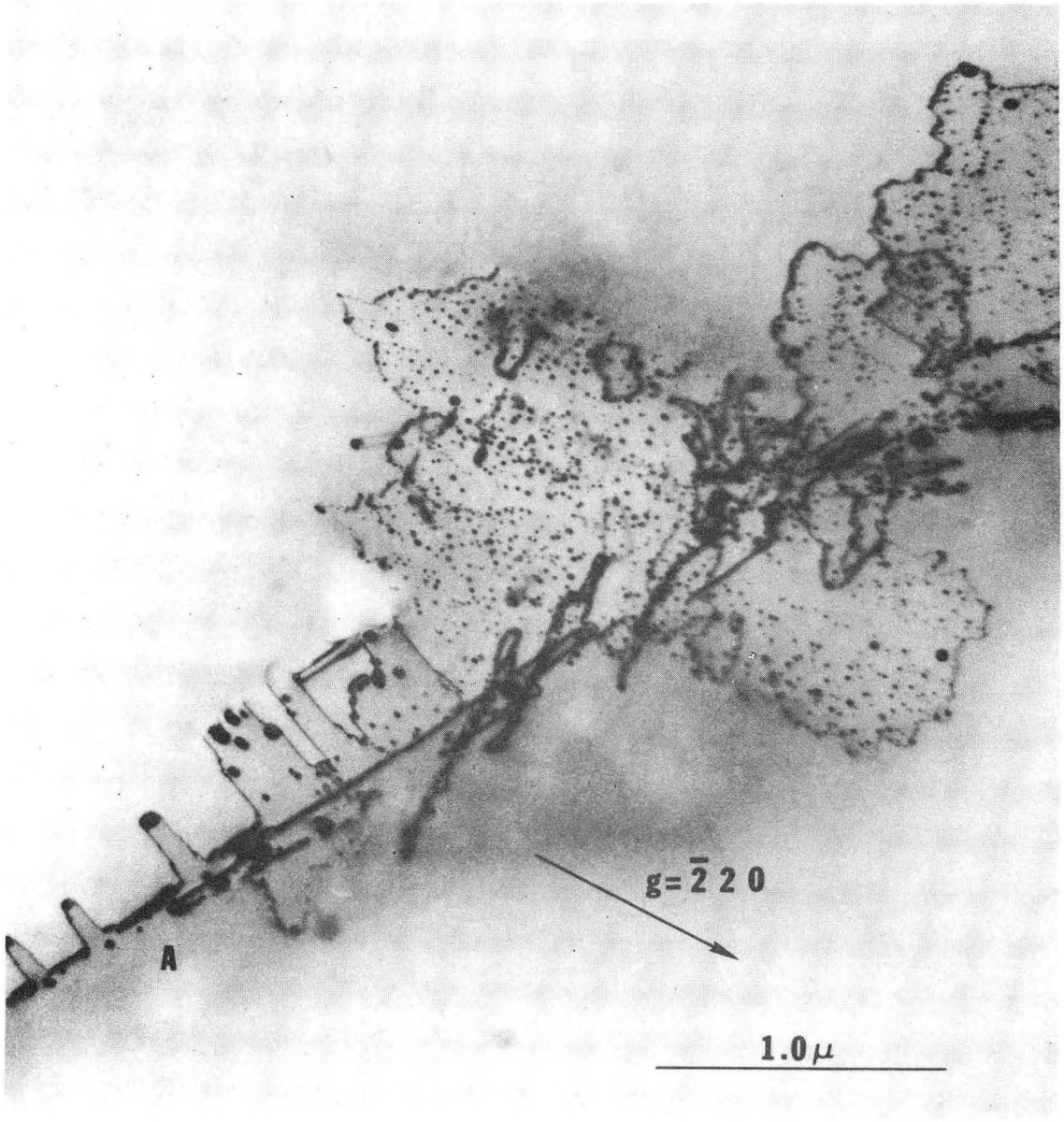

XBB 706-2842

Fig. 4

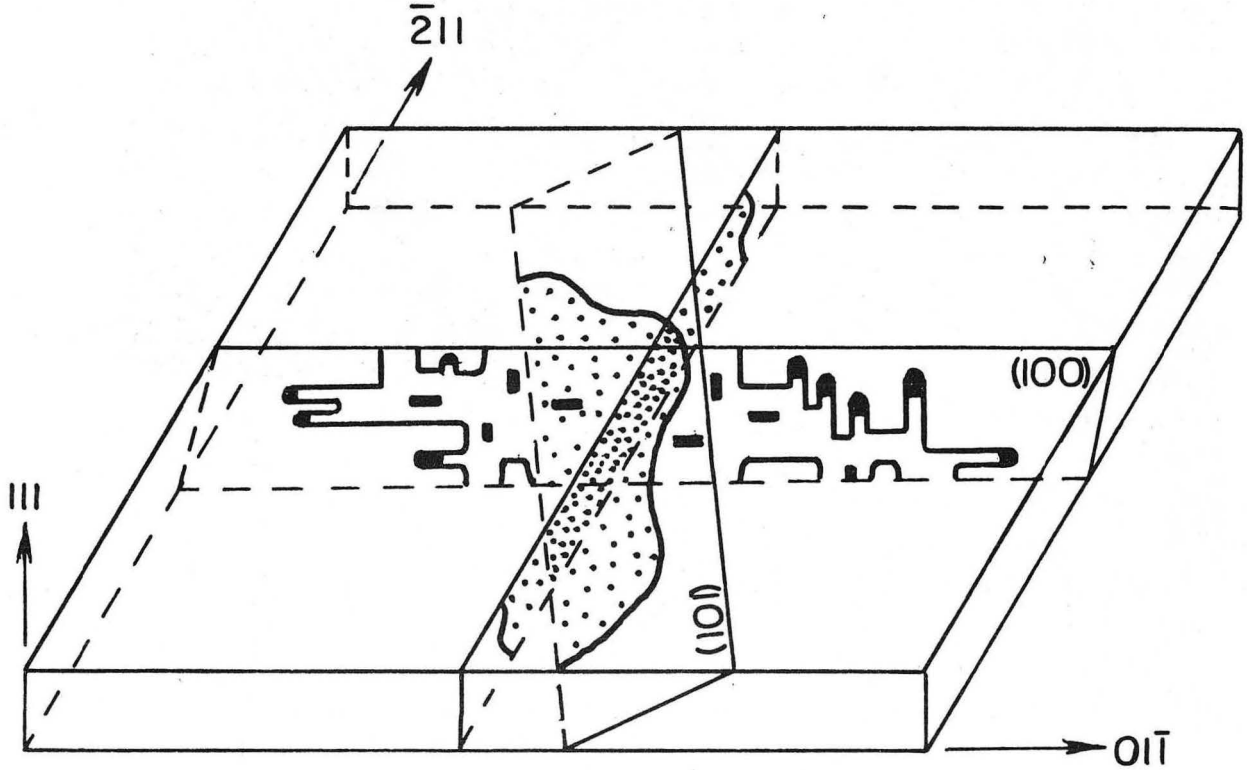

XBL 7010-6701

Fig. 5

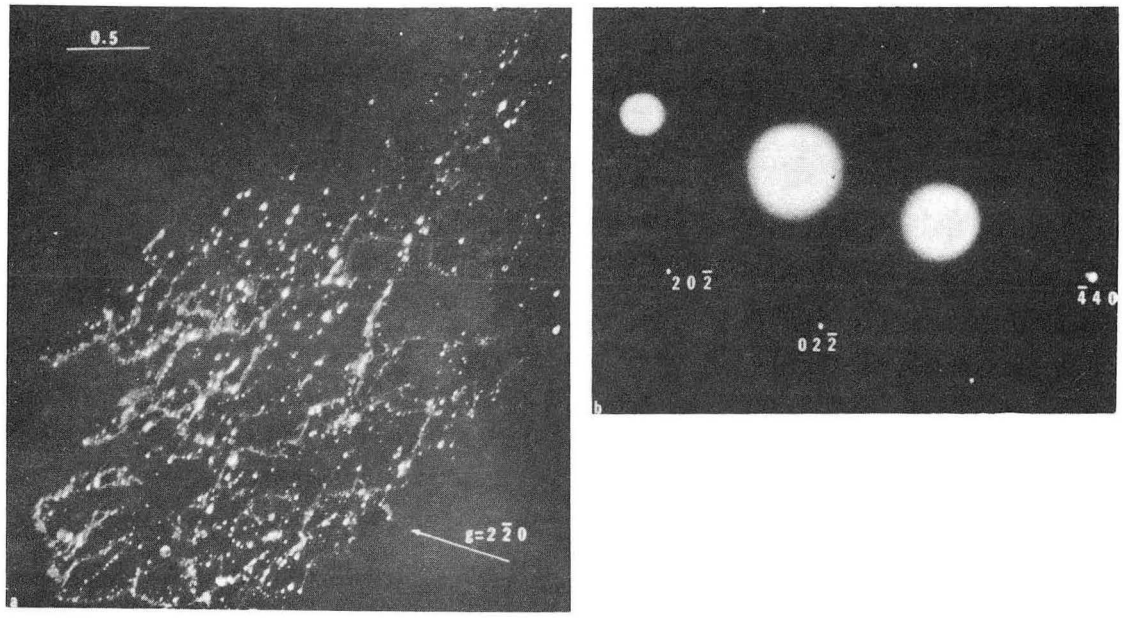

XBB 7011-5127

Fig. 6

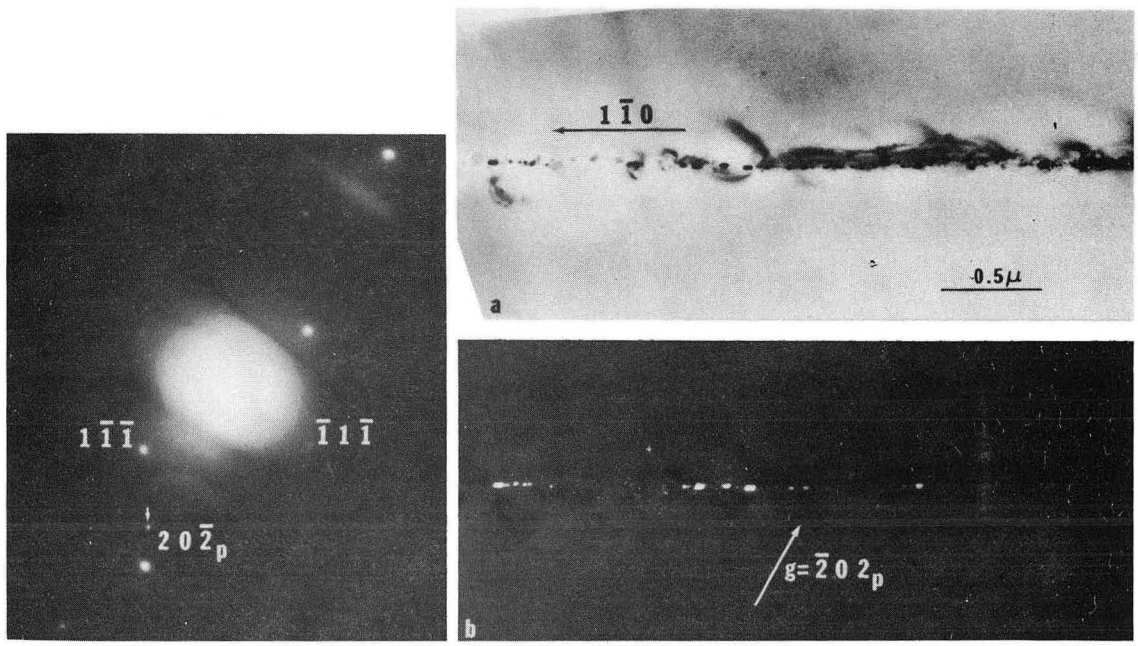

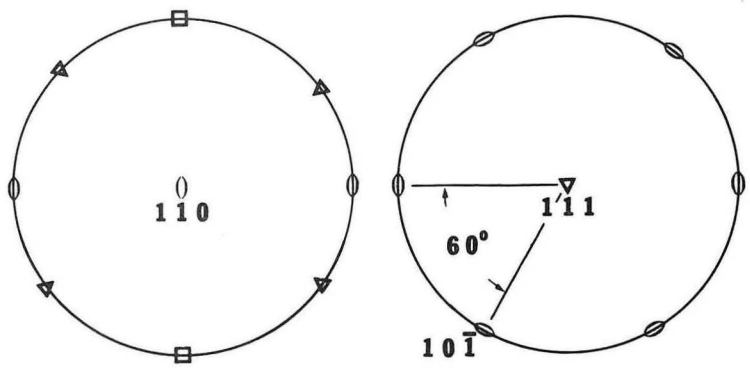

XBB 707-3133

Fig. 7

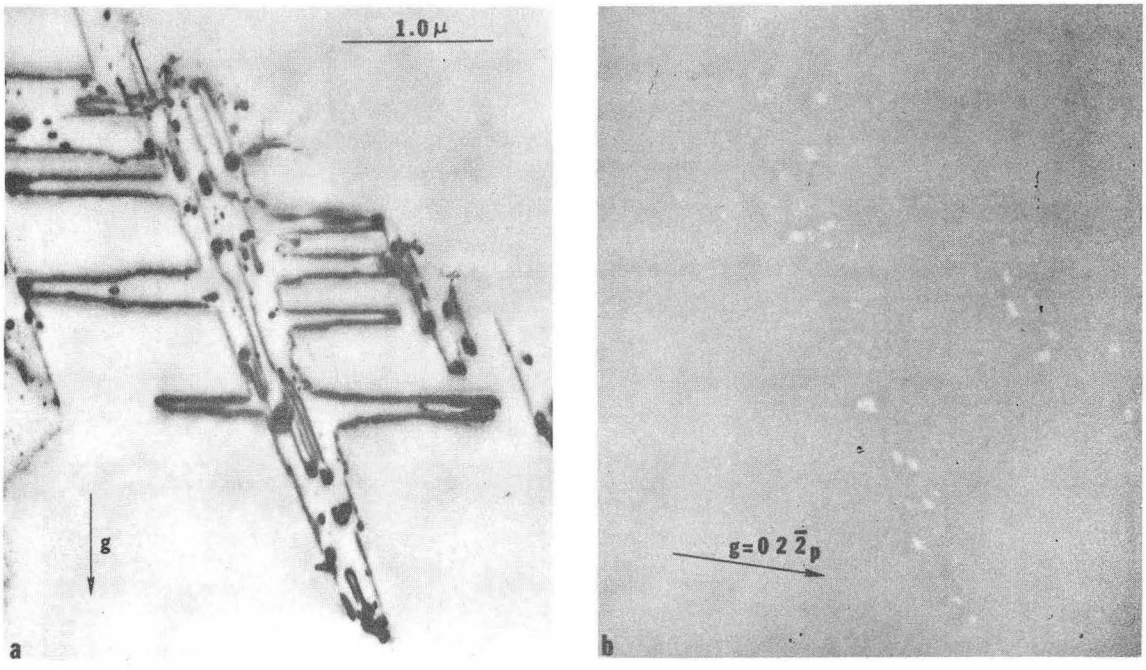

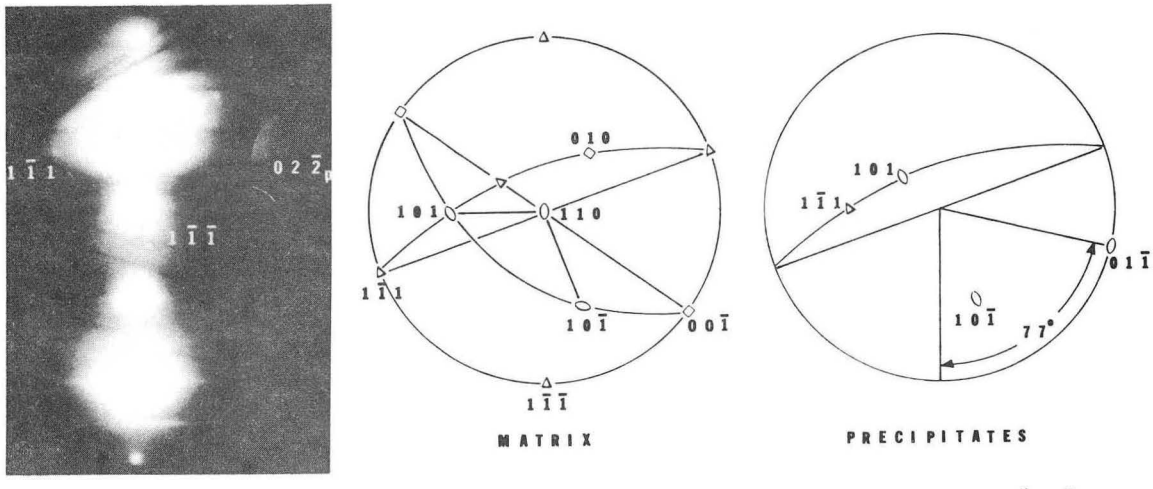

XBB 706-2833

Fig. 8

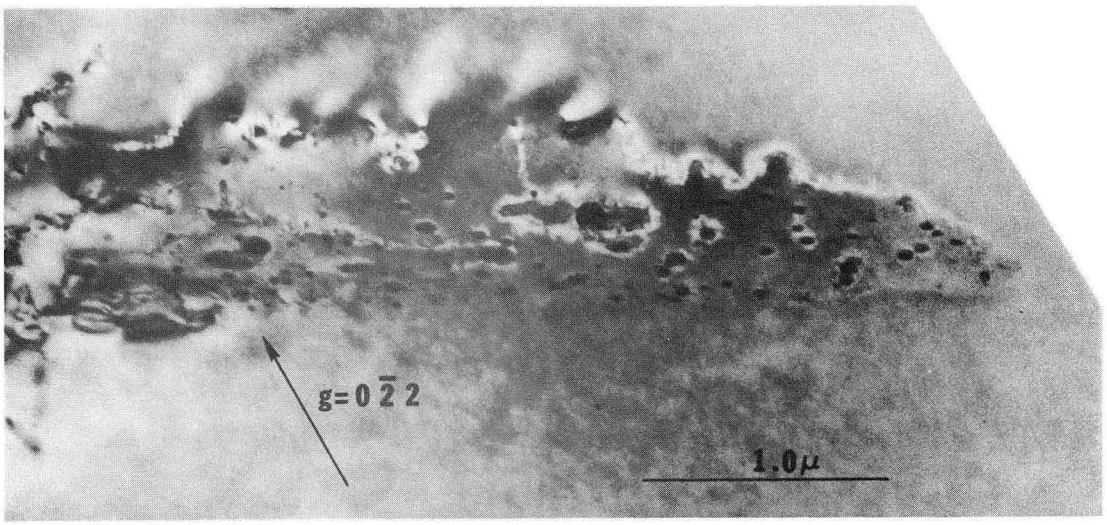

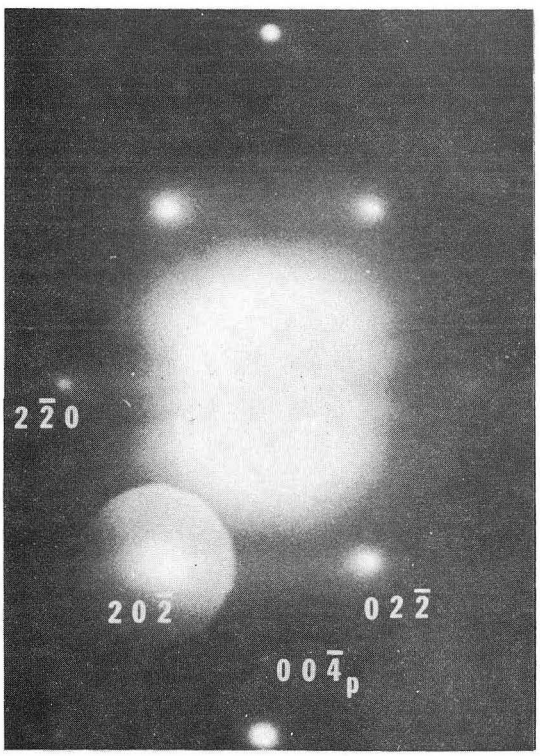

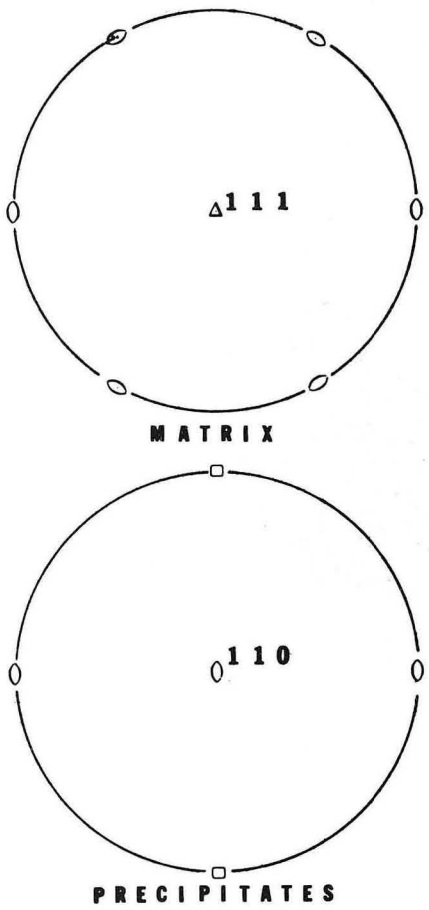

XBB 706-2832

Fig. 9

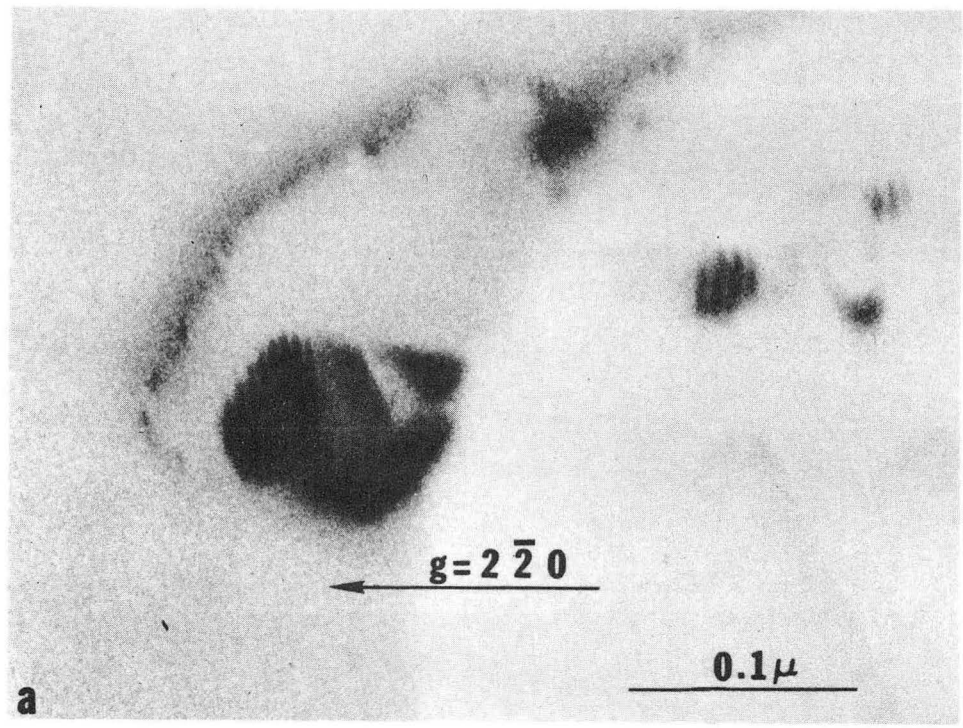

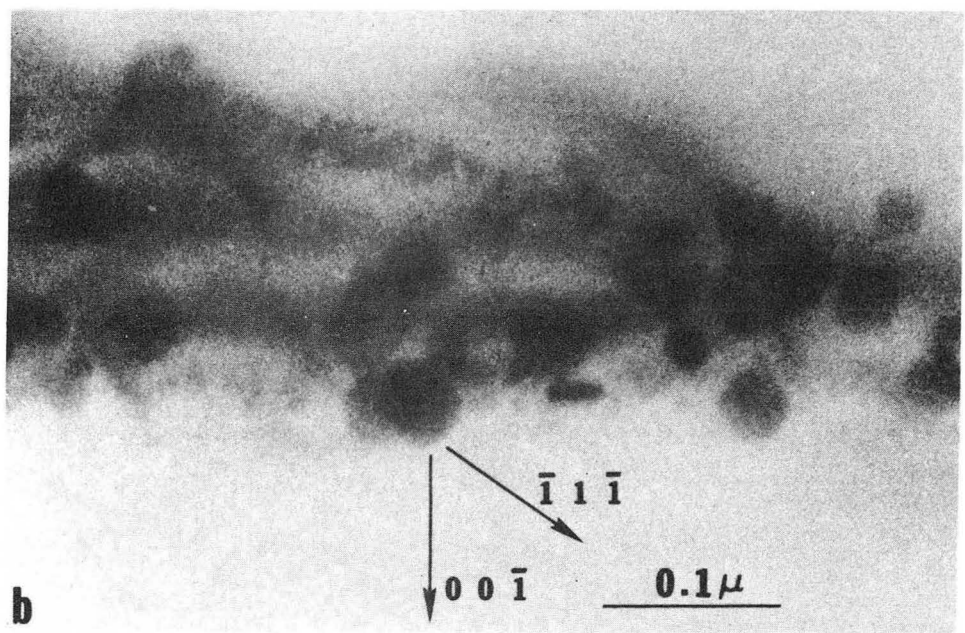

XBB 706-2836

Fig. 10

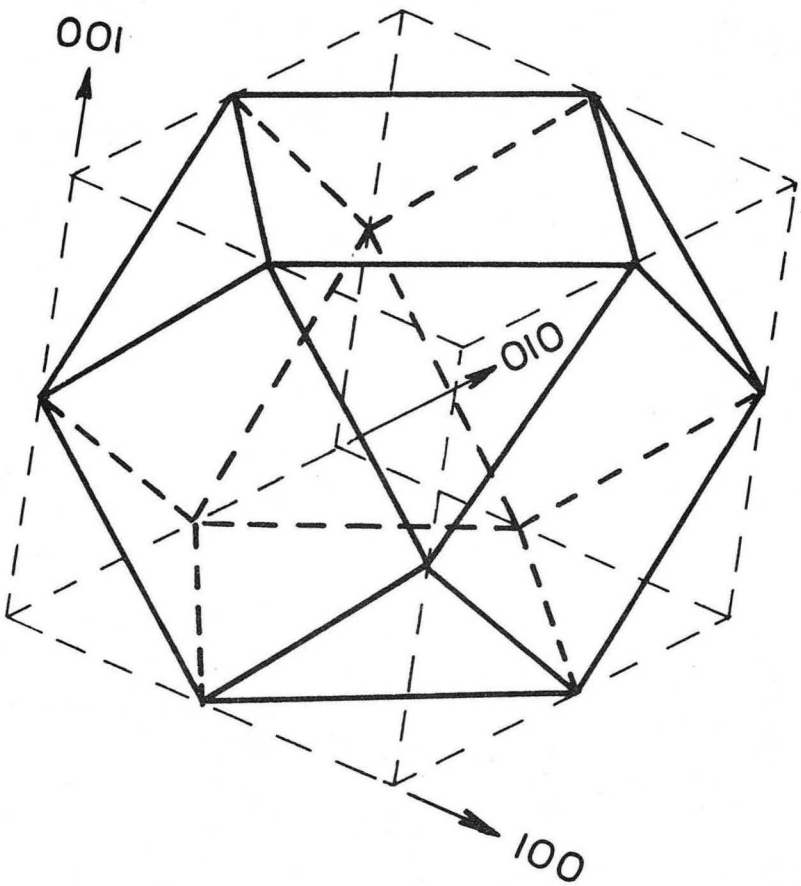

XBL 7010-6702

Fig. 11

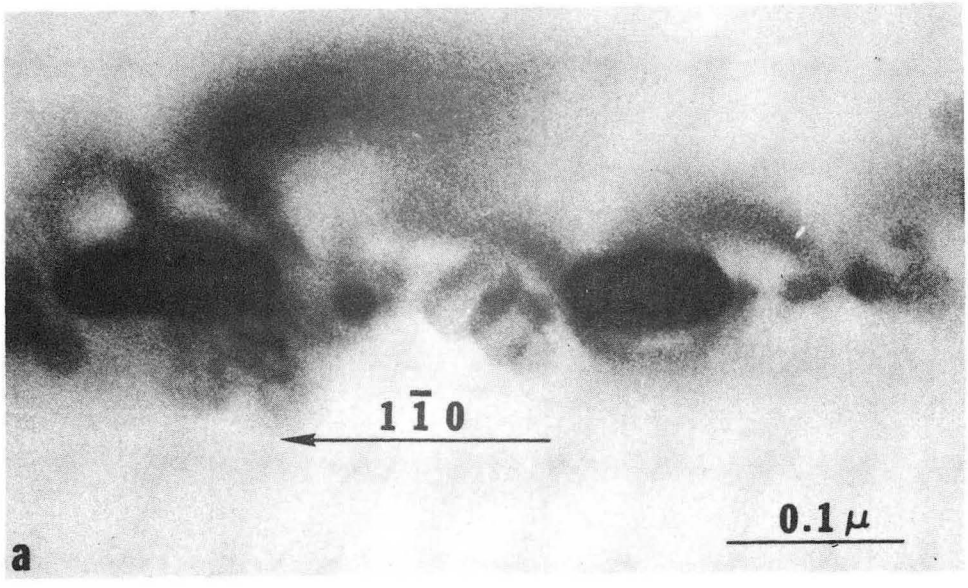

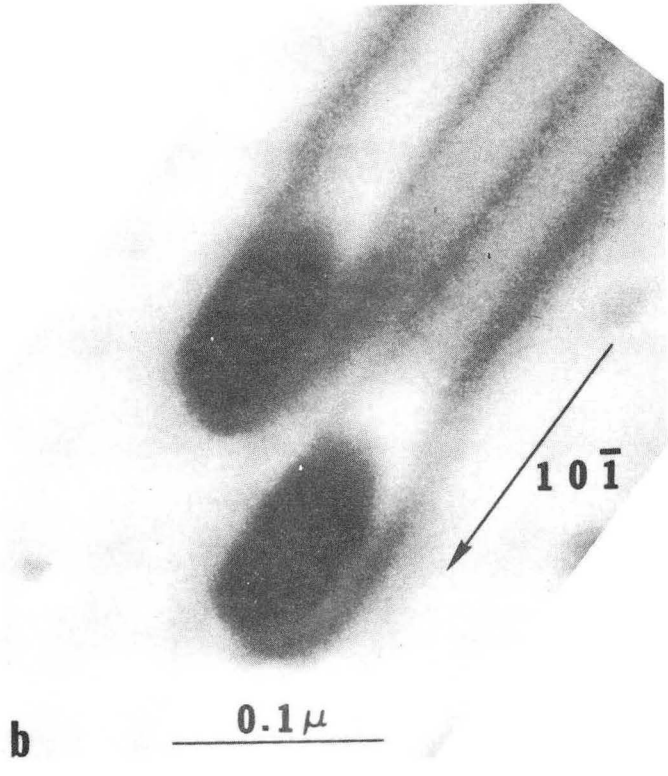

XBB 706-2838

Fig. 12

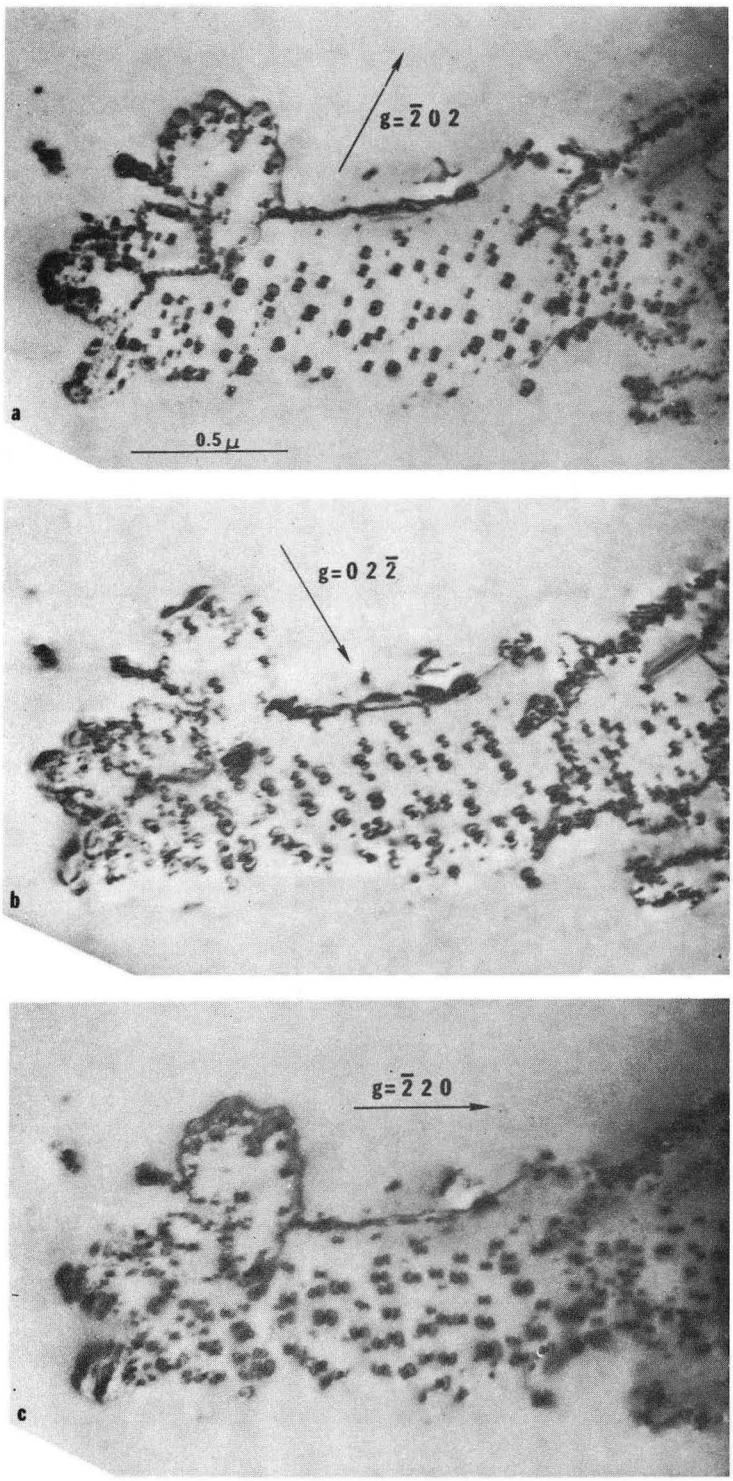

XBB 706-2850

Fig. 13

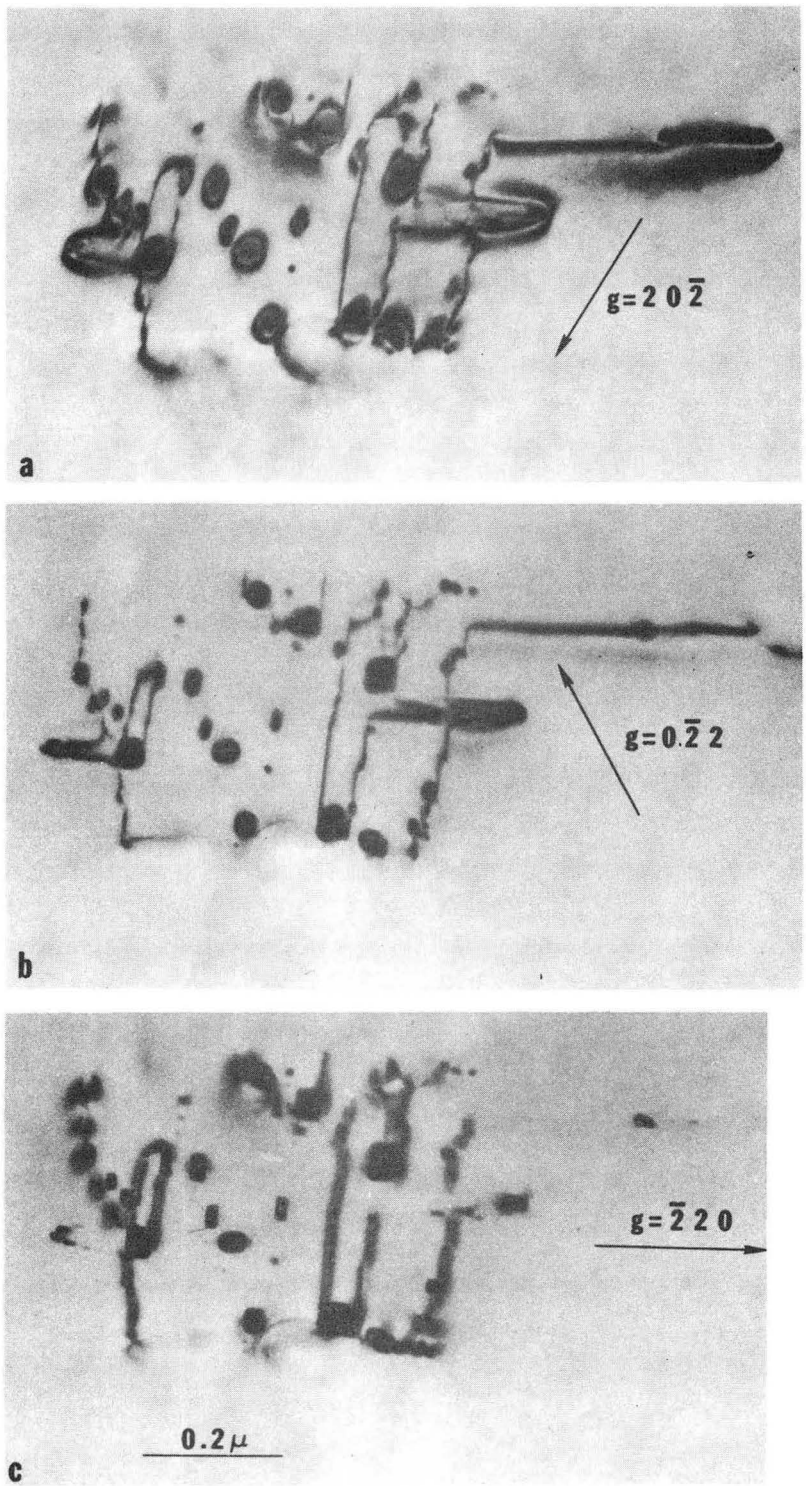

XBB 706-2845

Fig. 14

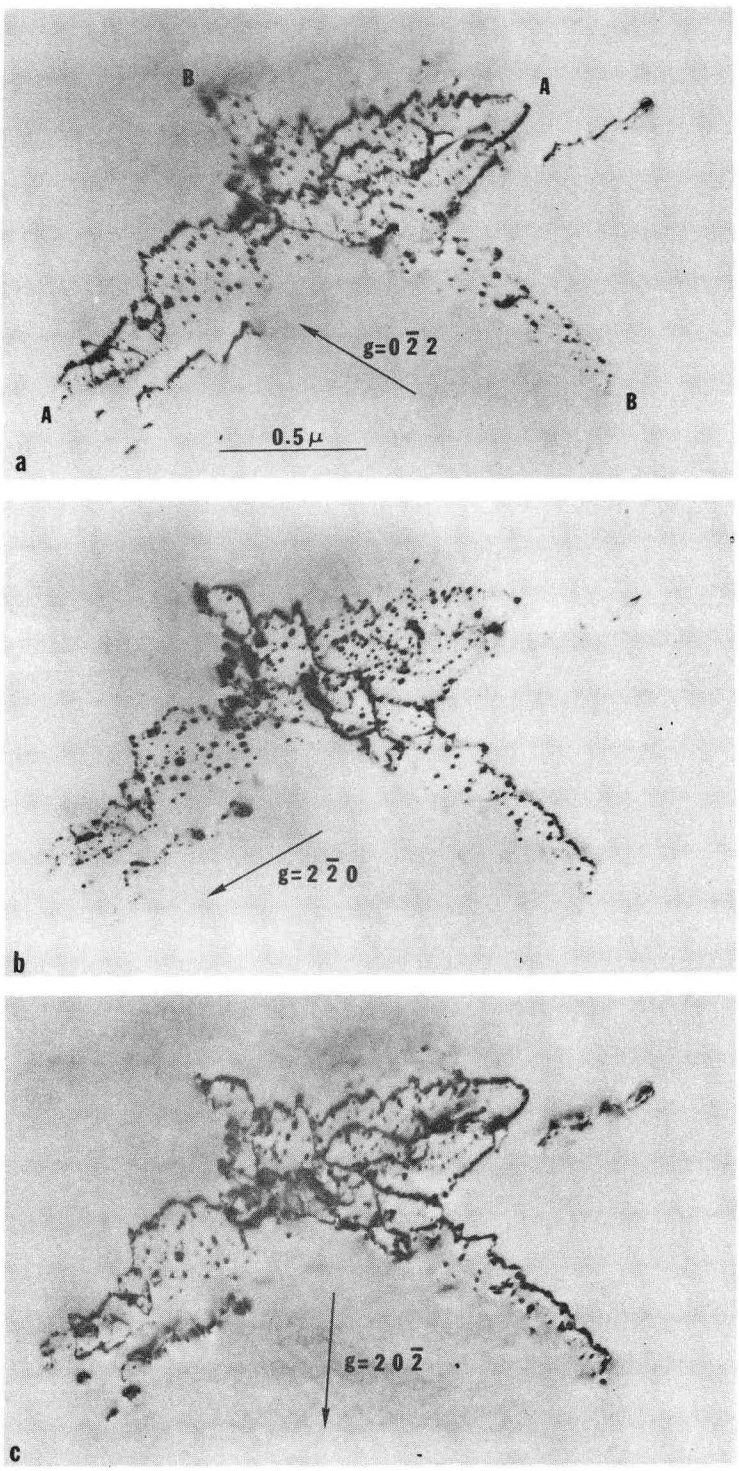

XBB 706-2847

Fig. 15

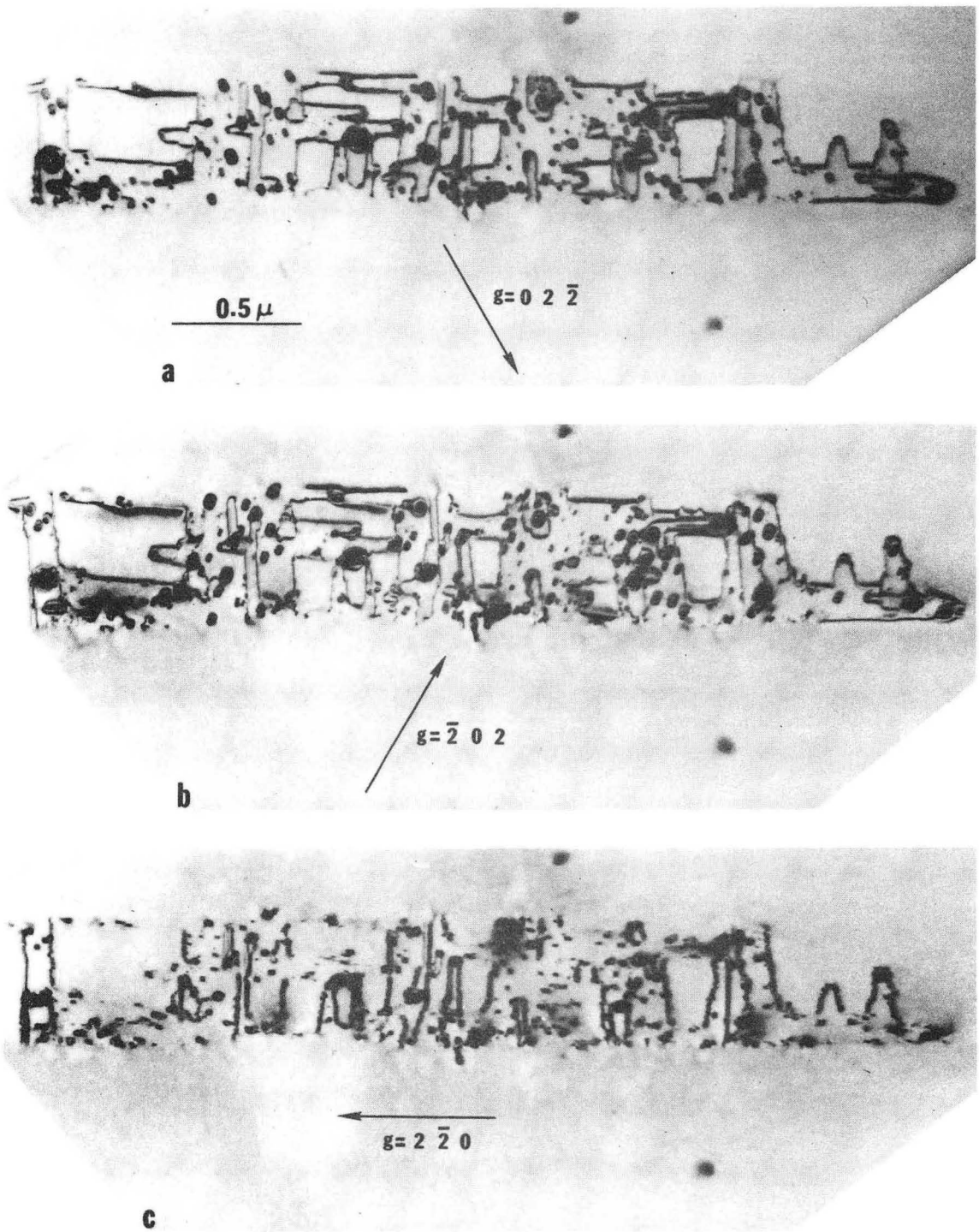

XBB 706-2841

Fig. 16

XBB 7011-5128

Fig. 17

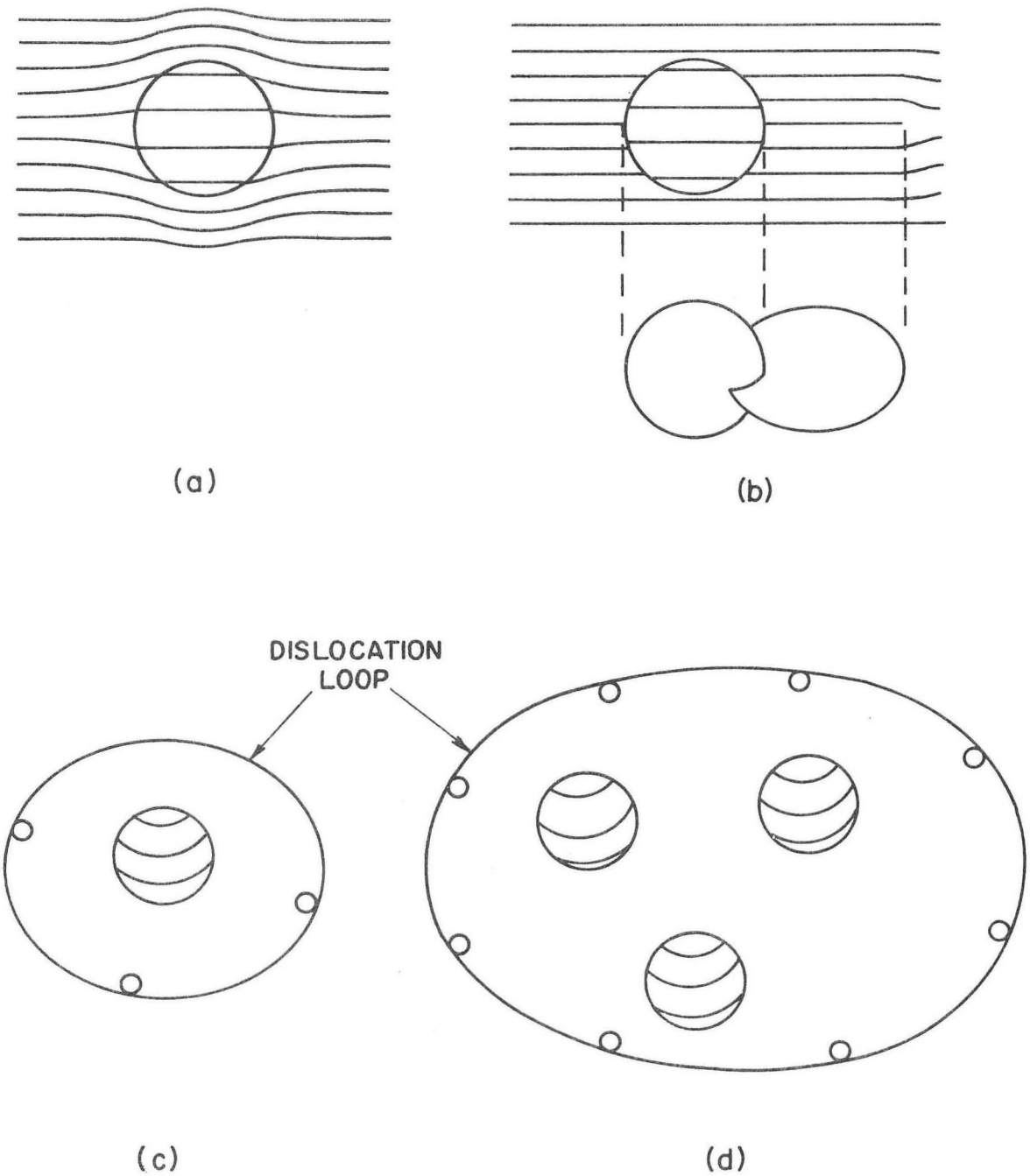

XBL 707-1565

Fig. 18

TECHNICAL INFORMATION DIVISION
LAWRENCE RADIATION LABORATORY
UNIVERSITY OF CALIFORNIA
BERKELEY, CALIFORNIA 94720